JACS
JOURNAL OF THE AMERICAN CHEMICAL SOCIETY

Article

pubs.acs.org/JACS

Carbon Nanodots: Toward a Comprehensive Understanding of Their Photoluminescence

Volker Strauss,[†,#] Johannes T. Margraf,[†,‡,#] Christian Dolle,[§] Benjamin Butz,[§] Thomas J. Nacken,[∥] Johannes Walter,[∥] Walter Bauer,[⊥] Wolfgang Peukert,[∥] Erdmann Spiecker,[§] Timothy Clark,[‡] and Dirk M. Guldi*[,†]

[†]Department of Chemistry and Pharmacy & Interdisciplinary Center for Molecular Materials (ICMM), Friedrich-Alexander-Universität Erlangen-Nürnberg, Egerlandstr. 3, 91058 Erlangen, Germany

[‡]Computer-Chemie-Centrum & Interdisciplinary Center for Molecular Materials (ICMM), Friedrich-Alexander-Universität Erlangen-Nürnberg, Nägelsbachstr. 25, 91058 Erlangen, Germany

[§]Center for Nanoanalysis and Electron Microscopy (CENEM), Friedrich-Alexander-Universität Erlangen-Nürnberg, Cauerstraße 6, 91058 Erlangen, Germany

[∥]Institute of Particle Technology (LFG), Friedrich-Alexander-Universität Erlangen-Nürnberg, Cauerstraße 4, 91058 Erlangen, Germany

[⊥]Lehrstuhl Organische Chemie II, Friedrich-Alexander-Universität Erlangen-Nürnberg, Henkestr. 42, 91054 Erlangen, Germany

Supporting Information

ABSTRACT: We report the characterization of carbon nanodots (CNDs) synthesized under mild and controlled conditions, that is, in a microwave reactor. The CNDs thus synthesized exhibit homogeneous and narrowly dispersed optical properties. They are thus well suited as a testbed for studies of the photophysics of carbon-based nanoscopic emitters. In addition to steady-state investigations, time-correlated single-photon counting, fluorescence up-conversion, and transient pump probe absorption spectroscopy were used to elucidate the excited-state dynamics. Moreover, quenching the CND-based emission with electron donors or acceptors helped shed light on the nature of individual states. Density functional theory and semiempirical configuration-interaction calculations on model systems helped understand the fundamental structure−property relationships for this novel type of material.

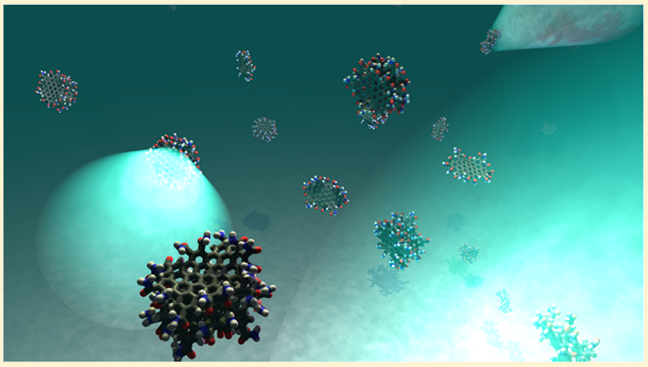

INTRODUCTION

A wide range of carbon nanomaterials such as reduced graphene oxide, graphene quantum dots, carbon nanodots (CNDs), partially reduced graphene, etc. exhibit optical properties that appear similar if not even identical.[1−3] One of the most striking features is their strong photoluminescence, which has led to their use in bioimaging and lighting.[4−6] The origin of this luminescence is, however, unclear, because these materials are often difficult to characterize.

A number of recent studies have contributed to the understanding of this phenomenon. Sun and co-workers have, for example, demonstrated photoinduced electron transfer between CNDs and toluene and aniline derivatives and have highlighted the involvement of trap states in such processes.[7] Likewise, the electroluminescence of CNDs has also been connected to trap states.[8] Recently, attention has shifted to single-particle spectroscopy with CNDs. This has revealed particles with single and multichromophoric characteristics, depending on the synthesis and/or post-treatment conditions.[9,31] Time-resolved spectroscopy suggests surface states to be the origin of luminescence in the different carbon materials.[10]

Pan and co-workers have reported a fairly narrow luminescence for graphene quantum dots with a narrow size distribution that is independent of the excitation wavelength. This suggests that size-confinement effects similar to those seen in inorganic quantum dots may be operative.[11] Heteroatoms are often incorporated into carbon nanostructures as a way to tune their optical properties.[12] For instance, XPS studies and elemental analysis show that the photoluminescence quantum yield correlates with the nitrogen content.[29,30] These observations have triggered a controversial debate as to how far quantum confinement and/or chemically distinct surface states contribute to the optical properties, in general, and luminescence, in particular, of these particles.[7,13,14]

Received: October 3, 2014
Published: November 5, 2014

   dx.doi.org/10.1021/ja510183c | J. Am. Chem. Soc. 2014, 136, 17308−17316

An adequate understanding of excited-state dynamics and structure−property relationships is pivotal for the rational design of carbon nanomaterials. We therefore now describe fully fledged photophysical assays conducted with newly synthesized CNDs that feature narrow, excitation-independent luminescence characteristics. These experiments are coupled to comprehensive theoretical analyses of the CNDs' optical properties. In considering a range of different model systems, we provide the basis for interpreting the experimental data, especially the role of trap states, with respect to the origin of CND-luminescence.

RESULTS AND DISCUSSION

Synthesis. In a typical synthesis, 0.75 g each of citric acid and urea were dissolved in 2.5 mL of deionized water. This solution was heated in a microwave reactor for 5 min. The temperature was controlled to maintain a pressure of 15 bar; see Experimental Section details. These conditions afforded deeply blue-colored solutions. This coloration likely stems from the formation of a polymer prior to the nucleation of CNDs. Under UV illumination, the solution exhibits bright blue fluorescence.

Pressure control limits the escape of gaseous byproducts from the solution, causing CND formation to terminate at an early stage. To corroborate this hypothesis, we performed experiments in an open container using an 800 W domestic microwave, as published by Wang et al.[15] Under these conditions no blue coloration is observable.

The precursor polymer readily hydrolyzes to a yellow, almost translucent solution; see Figure S1 (Supporting Information). This process does not, however, affect the blue luminescence. In the following we will refer to samples synthesized under pressure as pCNDs and to those synthesized under ambient conditions, that is, in a domestic microwave, as aCNDs.

Structural Characterization. Next, we turned to the structural characterization of pCNDs. In the powder X-ray diffraction (XRD, using Cu-Kα radiation (1.54 Å), $\Theta-2\Theta$ geometry) spectrum of pCNDs, a broad peak centered at approximately 25° is discernible, indicating the presence of nanosized and relatively disordered structures. We infer the presence of aromatic sp^2 carbons and amide groups from infrared (IR) spectroscopy, Figure S2. In addition, the measured ζ-potential value of -20.5 ± 0.6 mV suggests the presence of negative charges at the pCND surface, most likely in the form of carboxylate groups; see Figure S3.

Complementary insights into the structures of pCND and aCND came from thermogravimetric analysis coupled with mass spectrometry (TGA-MS) measurements; see Figure S4. Both samples release weakly physisorbed water in the range from 100 °C onward. In addition, pCNDs display a first significant mass loss related to NH^- ions at around 160 °C. Because this mass loss is less pronounced for aCNDs, we infer that pCNDs contain more of these nitrogen-containing functional groups. At temperatures above 180 °C, both aCNDs and pCNDs eliminate CO_2. It is safe to conclude that the general chemical structures of aCND and pCND are similar.

^{1}H and ^{13}C NMR analyses (liquid and solid state) of pCNDs confirm the presence of carbons stemming from carboxylates and amides, Figures S5−S8 in the Supporting Information. Furthermore, the peaks in the region between 148 and 157 ppm provide evidence for aromatic carbon atoms attached to strongly electron-withdrawing groups. No signals for protonated aromatic ring carbons were detected.

Analytical Ultracentrifugation. pCNDs were subjected to sedimentation velocity analytical ultracentrifugation (SV-AUC) experiments to obtain the sedimentation (s) and diffusion (D) coefficients. These are linked to the size of the CNDs. AUC analyses yielded an extremely narrow distribution for s and D, from which we conclude the presence of one major species. A contour plot of the data obtained is shown in Figure 1. The mean values are 0.236×10^{-13} s for s and 6.949×10^{-6} cm^2 s^{-1} for D.

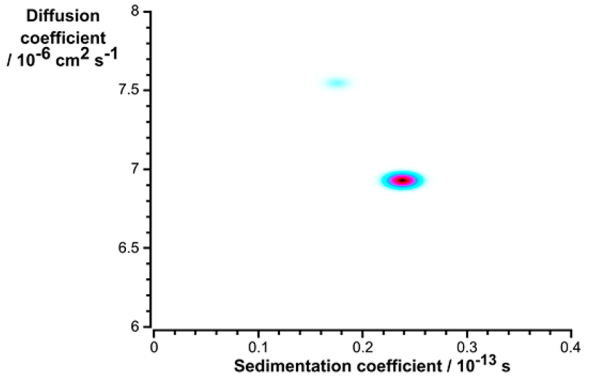

Figure 1. Pseudo-3D plot of the SV-AUC data demonstrating their narrow distribution in s and D. Intensity rises from white to blue and to red.

The sedimentation and diffusion coefficients, s and D are linked by the Stokes−Einstein relation to the size of the CNDs. Assuming a spherical shape, an average diameter of 0.62 nm is obtained from the s- and D-values. An alternative equivalently sedimenting spherical-particle treatment gives a particle diameter of 0.92 nm assuming a density of 1500 kg m^{-3} typical for carbon allotropes.[16] In short, AUC experiments lead us to conclude that pCND have diameters of slightly less than 1 nm and a remarkably narrow size distribution.

Microscopy. Structural characterization by high-resolution transmission electron microscopy (HRTEM) gave no indication of crystalline particles, in accordance with the XRD data; see Supporting Information and Figure S10. Considering the small particle sizes observed in the AUC studies, it is unlikely that defined crystalline phases will be observed. This is also evident in electron-diffraction experiments, where no diffraction of crystallites was observed. Amorphous agglomerates, on the other hand, exhibit too little mass−thickness contrast to be detectable in HRTEM. Owing to its size and composition, the nature of the material can be best described as weakly ordered. In fact, small ordered patterns of conjugated carbon are commonly found in the carbon support film.

To confirm AUC and HRTEM pCNDs were subjected to atomic force microscopy (AFM). The heights of 1100 objects were statistically evaluated for calculation of the height distribution shown in Figure 2 giving rise to particles with a mean height of 1 nm (see a representative AFM image in Figure S11). In addition, larger particles with heights up to 9 nm were found. Regarding the latter, their inhomogeneous structures and size distributions as well as the results from AUC suggest that these are, however, aggregates of smaller sized particles.

dx.doi.org/10.1021/ja510183c | J. Am. Chem. Soc. 2014, 136, 17308−17316

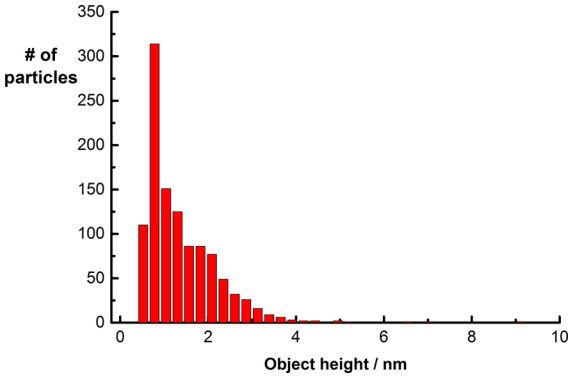

Figure 2. Size distribution from analysis of the AFM images for a total of 1100 objects.

Mechanism. The structural and microscopic characterization indicates the formation of nanosized, heavily functionalized sp^2 systems. Generally, carbonization processes are radical mediated polymerization reactions.[32,33] For example, in polyacrylonitril fibers thermally induced cross-linking, aromatization and rearrangement of heteroatom containing groups start at temperatures as low as 350 °C.[34] Urea is known to form aromatic oligomers upon thermal decomposition.[35] We assume that the high precursor concentration and rapid heating allow the polymerization and carbonization reactions to take place. Preorganization of the precursor molecules due to hydrogen bonding may also support this process. Further computational and experimental studies in this direction are planned.

Spectroscopic Characterization. After work up, the absorption spectrum of pCNDs gives rise to a single, well-defined absorption maximum at 342 nm (λ_{abs}). Here, comparison with aCNDs is instructive. aCNDs display a second, broad peak around 410 nm, which is accompanied by a tail throughout the entire visible region, Figure S12. The luminescence spectrum of pCNDs, Figure S12, exhibits a narrow peak (fwhm = 69 nm) with a luminescence maximum at 445 nm (λ_{em}) in contrast to a rather broad peak (fwhm = 92 nm) found for aCNDs at 519 nm.

3D-luminescence plots reveal a single, relatively narrow luminescence maximum for pCNDs, whereas aCNDs give rise to the well-known excitation-dependent luminescence, Figures 3 and S13. Remarkably, for pCNDs the luminescence quantum yield is as high as 20% in water. Considering that the excitation spectra correspond to the absorption spectrum at any given

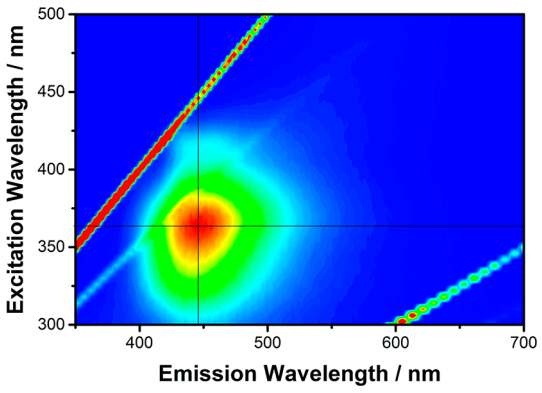

Figure 3. 3D-Luminescence plot of pCND in aqueous solutions at room temperature. Intensity rises from blue to green and to red.

luminescence wavelength, the luminescence appears to originate from a single pCND species, while at least two independent luminescent aCND species are present. Their high quantum yield and the homogeneous features render pCNDs ideal for in-depth photophysical characterization. We therefore focus our attention exclusively on the properties of pCNDs.

The temporal evolution of the pCND luminescence was investigated by time-resolved emission spectroscopy (TRES) with measurements in the range from 400 to 550 nm, Figure S14. Here, multiwavelength analyses indicate that the luminescence decay is rather heterogeneous throughout the measured range. In particular, the luminescence tends to be longer lived in the blue region, that is, around 400 nm, than in the red, that is, around 550 nm with average lifetimes of 2.2 and 7.2 ns, respectively. As a complement, time-correlated single-photon counting (TCSPC) measurements were carried out with pCNDs. These measurements afford luminescence time profiles that are best fit by triexponential fitting functions yielding lifetimes of 1.9, 5.4, and 8.8 ns. This suggests either several competing deactivation pathways within the same particles, simultaneous luminescence from different particles, or a broad dispersion of recombination rates due the same process. Nevertheless, we infer the presence of ultrashort components, which are masked by the temporal resolution of the instrument.

To obtain insights into the pCND luminescence dynamics on a time scale shorter than TCSPC, we turned to fluorescence up-conversion spectroscopy. Representative luminescence spectra taken at different time delays in the wavelength range from 410 to 510 nm, and luminescence time profiles at 440, 460, and 480 nm are shown in Figure 4. Independent of the

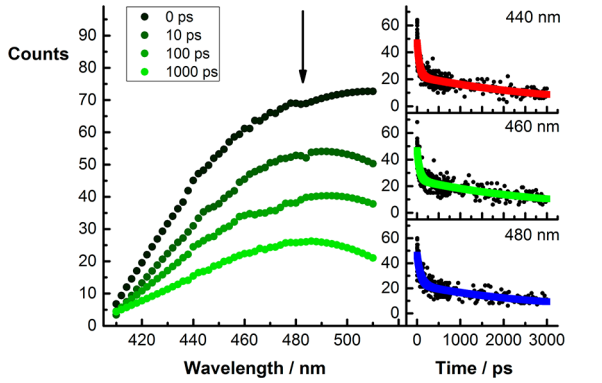

Figure 4. Left: Fluorescence up-conversion spectra obtained upon excitation (387 nm) of pCND in aqueous solutions with several time delays between 0 and 1000 ps at room temperature. Right: Time-luminescence profiles of the spectra shown on the left at 440, 460, and 480 nm.

wavelength, we note in the luminescence spectra a rapid decay of ~68 ps followed by a long decay of >3 ns. In line with the conclusions drawn from TRES, Figure S14, the 3 ns component dominates the long-wavelength regime. In contrast, the short-lived component on the ps time scale is more pronounced in the short-wavelength regime. For instance, the relative ratio at 440 nm is 71:29, while at 480 nm it is 38:62.

Finally, femtosecond transient absorption measurements were carried out with pCND to corroborate the aforementioned findings and to obtain further information about the excited-state dynamics. Figure S15 illustrates that upon 387 nm photoexcitation, pCNDs give rise to differential absorption

dx.doi.org/10.1021/ja510183c | J. Am. Chem. Soc. 2014, 136, 17308−17316

changes that are rather broad and range from 450 to 700 nm. From multiwavelength analyses, the major decay components were derived by means of biexponential fittings as 0.9 and 6.5 ps.

Still, the differential absorption changes and the absorption time profiles indicate the presence of an additional long-lived component, which is persistent on the time scale of the femtosecond experiments.

Our fully fledged excited-state lifetime analyses by means of TRES, TCSPC, fluorescence upconversion, and transient absorption yield a set of three short-lived components on the ps time scale and three long-lived components on the ns time scale, see Table 1, which is illustrated schematically in Figure 9.

Table 1. Excited State Lifetimes of pCND in Aqueous Solutions at Room Temperature[a]

1	2	3	4	5	6	7
TRES						
				3.3 ns (24%)	7.4 ns (76%)	
TCSPC (λ_{ex} = 403 nm)						
			1.9 ns (14%)	5.8 ns (62%)	8.8 ns (25%)	
Fluoresence up-conversion (λ_{ex} = 387 nm)						
		63 ps (56%)		3.5 ns (44%)		
Transient absorption (λ_{ex} = 387 nm)						
0.1 ps (96%)					>5 ns	
3.4 ps (4%)						

[a]The numbers in the top are analogous to Figure 9.

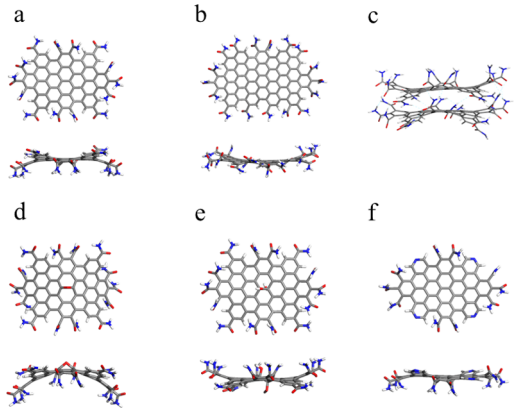

Figure 5. ωB97X-D/def2-SV(P) (B97D for the dimer) optimized geometries of CND model systems. (a) CND1, (b) CND2, (c) $CND1^{bilayer}$, (d) $CND1^{epoxy}$, (e) $CND1^{hydroxy}$, (f) $CND1^{pyridine}$.

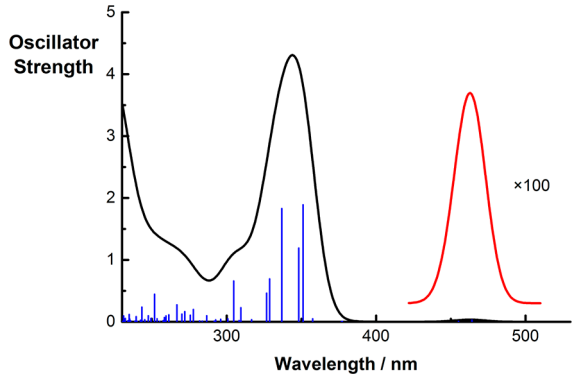

Figure 6. UNO-CIS simulated absorption spectrum of CND1.

In accordance with the literature on CNDs, on one hand, and on excited-state dynamics in quantum confined systems, on the other, we correlate the short lifetimes with the population of trap states and/or exciton formation, while the long lifetimes relate to intrinsic and trap-mediated luminescence processes.

Molecular Modeling. Density functional theory (DFT) and semiempirical unrestricted natural orbital-configuration interaction (UNO-CI) calculations on CND model systems were used to study possible relationships between structure and optical properties. The basic assumption on which we based the construction of a suitable model system was that the optical properties of CNDs originate from an sp^2-carbon network.

We constructed two differently sized, amide-capped graphene ribbons (CND1 and CND2), and a bilayer of CND1. To study the possible chemical origin of trap states, we also considered chemical modifications of the sp^2-network of CND1 such as epoxidation, hydroxylation of a central double bond, and existence of pyridinic nitrogens at the edges of the lattice. In total, we created six different model systems, whose ωB97X-D/def2-SV(P) optimized geometries are shown in Figure 5.[17,18]

The experimental pCND IR-spectra are in sound agreement with the one simulated for CND1, Figure S16. This is an important indication of the realistic character of the model systems. Optical properties of the models were calculated using the unrestricted natural orbital-configuration interaction singles method (UNO-CIS)[19] with the PM3 Hamiltonian.[20] The simulated absorption spectra also match the experimental spectrum, Figures 6 and S17–S22. In Table S1, some key properties from these simulations are listed for all models. In particular, the wavelengths of the fundamental absorption maximum (λ_{abs}) and the lowest-energy excited state (λ_{em}), and the rate of radiative decay for this state (k_r). λ_{em} and k_r are of interest because in principle they indicate both the energetic disposition and the rate and intensity of an expected emission, according to Kasha's rule.

Despite their large π-systems, all models are nonplanar. The high degree of functionalization of their edges causes out-of-plane distortions of the sp^2-networks. The structure of CND1 bilayers is mainly governed by hydrogen-bonding interactions between the surface amide groups. The resulting interlayer spacing of 4.2 Å is markedly larger than the van-der-Waals contact distance between two carbon atoms, indicating that the bilayer is not a classical π-stacked dimer. Still, even at such separations some weak interlayer electronic interactions are likely to occur.

Increasing the particle size from CND1 to CND2 leads to red-shifted absorption and luminescence bands and increased rates of radiative decay. The latter nearly reaches 2 orders of magnitude. Formation of a bilayer results in a red-shift of λ_{em}, and a decrease in k_r. λ_{abs} is blue-shifted, contrary to what is usually expected for aggregates.

Similarly, chemical modifications affect the predicted optical properties. Epoxidation imposes a strong distortion of the sp^2-framework. This is accompanied by a blue shift in absorption and emission and an increase in k_r. Transhydroxylation has the opposite effect. Absorptions and emissions are red-shifted, while k_r decreases. Notably, $CND1_{hydroxy}$ also features a very

dx.doi.org/10.1021/ja510183c | J. Am. Chem. Soc. 2014, 136, 17308–17316

low-lying triplet state, only 0.38 eV above the singlet ground state; see Figure S23. Finally, pyridinic nitrogens localized at the edges of CNDs evoke the strongest blue shifts in the spectral features and an increased rate of radiative decay.

A more realistic description of the luminescence of the model system required, however, the conformational freedom of the structure to be taken into account. We therefore performed classical molecular-dynamics simulations of CND1 in water and at room temperature. From a 2 ns production run, we extracted 200 snapshot geometries. In the next step, we determined the variation of the lowest lying excited state in terms of energy and k_r by performing UNO-CIS calculations on each geometry, Figure S24. To simulate more extensive sampling, we placed Gaussian functions on each state (fwhm = 20 nm).

In this manner, we computed a luminescence spectrum spanning from 500 to 600 nm that is qualitatively similar to that of the experimental pCND luminescence. In particular, the sharp flank and the trailing luminescence in the blue and red regions of the spectrum, respectively, are well reproduced.

The rate of nonradiative decay is derived from the luminescence quantum yield, while the calculated Einstein coefficients yield the rate of radiative decay. By assuming a quantum yield of 0.2, the decay of the emissive band is simulated, Figure S25. From this simulation, average lifetimes between 5 and 10 ns evolve in the spectral range from 510 and 560 nm. Interestingly, the luminescence tail beyond 560 nm reveals lifetimes that are significantly longer.

Our theoretical analyses indicate that the luminescence of solvated, heavily functionalized sp^2-networks occurs throughout a broad energy range. The luminescence lifetime steadily increases on going from the blue to the red. Therefore, in contrast to the general view regarding inorganic quantum dots, the rather broad luminescence does not indicate a polydisperse sample in this case. Neither do the spectral width and observation of multiexponential luminescence decay indicate the presence of trap states. All states considered have clear $\pi-\pi^*$ character.

Simulations of chemically modified CNDs reveal that pyridinic nitrogen and epoxy-oxygen atoms cause a blue shift of the luminescence and an increased rate of radiative decay. Stacking and hydroxlation, on the contrary, lead to a red-shifted luminescence, which features decreased radiative decay rates. This shows that chemical defects of the sp^2 lattice can have diverse effects on the resulting optical properties.

A comparison of the experimentally determined pCND lifetimes and those simulated for CND1 shows reasonable agreement in the blue regime of the spectrum including the luminescence maximum region. In contrast, the simulated lifetimes at the red end of the spectrum deviate strongly. Here, the lifetimes decrease rather than increase relative to the blue part of the spectrum. Therefore, a competing decay mechanism not considered in the model apparently dominates the longer wavelength region. To probe the excited state nature of pCNDs further, we turned to luminescence quenching experiments with both electron donors and acceptors.

Photophysics: Electron-Donating Properties. Following their basic characterization in terms of microscopy and spectroscopy, photoexcited pCNDs were subjected to oxidative quenching experiments. We started with concentration-dependent luminescence experiments of pCNDs by adding as little as 10^{-4} and as much as 0.1 M of *N*,*N*-methylviologen (MV). Importantly, the luminescence was quenched quantitatively, that is, in excess of 99.9%, when MV^{2+} concentrations reached 10^{-2} M.

Stern–Volmer plots, in which the integrated luminescence intensity was plotted versus the quencher concentration, assisted in analyzing the luminescence quenching, Figure 7.

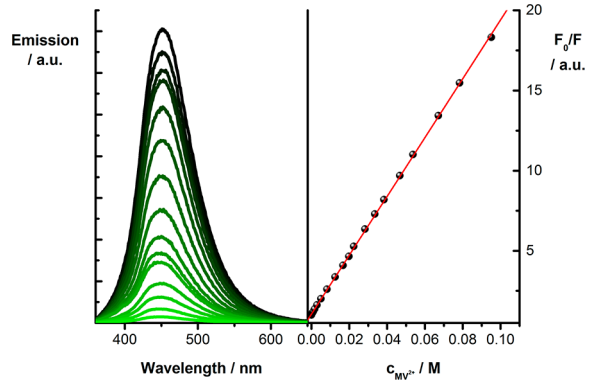

Figure 7. Left: Steady-state luminescence spectra of pCND with increasing amounts of MV^{2+} upon excitation at 350 nm. Right: Corresponding Stern–Volmer plot.

In doing so, we used the linear F_0/F versus MV^{2+} concentration dependence throughout the entire concentration range to derive a rate constant of 2.2×10^{-1} M $^{-1}s^{-1}$. This value exceeds, however, the kinetics of a purely diffusion-controlled process with 8.0×10^9 M^{-1} s^{-1} and, in turn, suggests a static rather than a dynamic picture.

ζ-potential measurements further confirm this hypothesis. In the absence of MV^{2+}, pCNDs feature a negatively charged surface. In the presence of variable MV^{2+} concentrations, the ζ-potential decreases and plateaus at around −8 mV, Figure S3.

From these findings we hypothesize that a preorganization of positively charged MV^{2+} and negatively charged pCNDs in the form of an electrostatically bound complex balances, at least, in part the negatively charged pCND surface and, in turn, dominates the overall pCND luminescence quenching. A closer look at the luminescence spectra in the absence and presence of 0.1 M MV^{2+} reveals a blue-shift of 4 nm in the luminescence spectra.

To probe the dynamics of luminescence quenching, MV^{2+} was added to pCNDs in TCSPC and fluorescence up-conversion experiments. The lifetimes obtained are summarized in Table 2. As mentioned above, the luminescence of pure pCNDs is best described by a three-component decay with lifetimes of 1.9, 5.4, and 8.8 ns.

Overall, the luminescence quenching as induced by MV^{2+} impacts all three of these lifetimes. In particular, the long-lived component of 9 ns is indiscernable, depending on the MV^{2+} concentration, while the medium component of 5 ns undergoes significant shortening and reduction in amplitude. The short-lived component of 1.9 ns is, on the one hand, further reduced to 1.1 ns at the highest MV^{2+} concentration, and, on the other, the only appreciable component left behind at, for example, 0.1 M MV^{2+}. In up-conversion measurements, the two lifetimes are reduced to 12.8 and 325 ps when 0.1 M MV^{2+} is added, Figures S26–S27 and Table 2.

From the luminescence quenching we infer that photoexcited pCNDs are susceptible toward an oxidative charge transfer owing to the lack of intrinsic and trap-mediated luminescence processes. To elucidate this aspect, we conducted femtosecond

dx.doi.org/10.1021/ja510183c | J. Am. Chem. Soc. 2014, 136, 17308–17316

Table 2. Excited State Lifetimes of pCND in Aqueous Solutions and in the Presence at 0.1 M MV^2 at Room Temperature[a]

1	2	3	4	5	6	7
TCSPC (λ_{ex} = 403 nm)						
			1.1 ns (77%)	0.5 ns (23%)		
Fluorescence up-conversion (λ_{ex} = 387 nm)						
				330 ps (52%)		13 ps (48%)
Transient absorption (λ_{ex} = 387 nm)						
0.3 ps (52%)	1.5 ps (39%)					8.8 ps (9%)

[a]The numbers in the top line are analogous to Figure 9.

transient absorption measurements with pCNDs in the absence and presence of MV^{2+}. Upon addition of MV^{2+} two new maxima not seen for bare pCNDs evolve at 620 and 660 nm in the differential absorption spectra. These maxima are assigned in accordance with the literature to the one-electron reduced form of MV^{2+}, that is, MV^{1+}, Figure 8.[21]

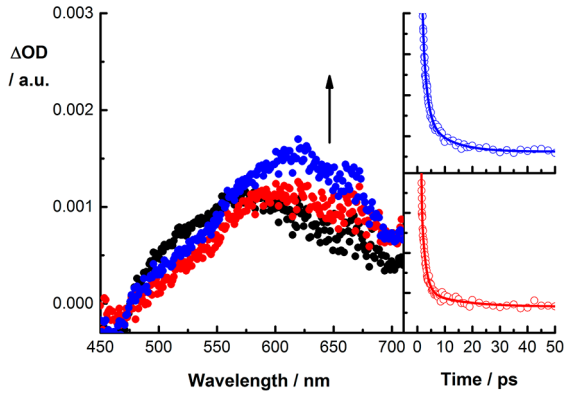

Figure 8. Left: Differential absorption spectra obtained upon femtosecond flash photolysis (387 nm) of pCND in aqueous solutions without (black), and upon addition of 0.01 M (red) and 0.1 M (blue) MV^{2+} with time delays of 5 ps at room temperature. Right: Time-absorption profiles of the spectra shown on the left at 625 nm.

The excited-state decays of pCNDs were fit in the absence and presence of different amounts of MV^{2+} by means of their characteristic features in the visible range and the corresponding lifetimes are summarized in Table 2. In addition to the short-lived and an intermediate-lived lifetime seen for pCNDs a third, longer-lived component evolves upon addition of MV^{2+}. Notably, in the presence of MV^{2+} the intermediate-lived component is shortened. Therefore, we relate the intermediate lifetime to charge separation, while the longer one correlates with charge recombination. The fact that the amplitudes of the lifetimes increase with increasing amounts of MV^{2+} and that the intrinsic ultrashort lifetime decreases simultaneously underpins this hypothesis. The immediate formation of the charge-separated state between pCNDs and MV^{2+} supports the notion of a preorganized complex. The photophysical processes of this quenching process are schematically shown in Figure 9.

Photophysics: Electron-Accepting Properties. As a complement to the above, we probed the electron-accepting properties of pCNDs in conjunction with electron-donating triethanolamine (TEOA). In this case, concentration-dependent luminescence quenching was studied in the range between 10^{-4} and 3 M TEOA. Luminescence spectra and the corresponding Stern–Volmer plots are shown in Figure 10.

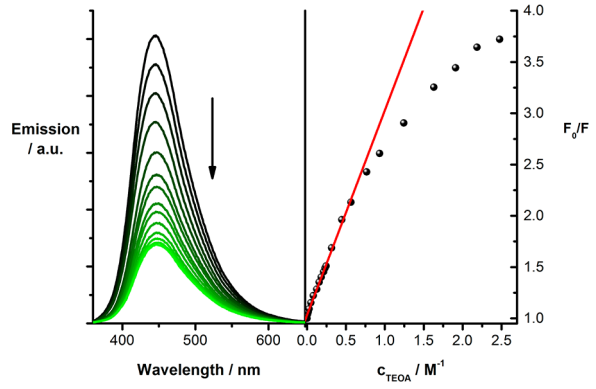

Figure 10. Left: Steady-state luminescence spectra of pCND with increasing amounts of TEOA upon excitation at 350 nm. Right: Corresponding Stern–Volmer plot.

As such, the luminescence quenching observed during the TEOA titrations plateaus at ~27%. In particular, at sub mM concentrations, no appreciable quenching is noted, while in the 0.001–0.5 M regime the quenching appears to be nearly linear before reaching a plateau at concentrations of ~3 M.

The Stern–Volmer quenching constant was derived in the low concentration regime to be 1.1×10^8 M^{-1} s^{-1}. This implies luminescence quenching, which is appreciably slower than diffusion control. To shed light onto this slower deactivation,

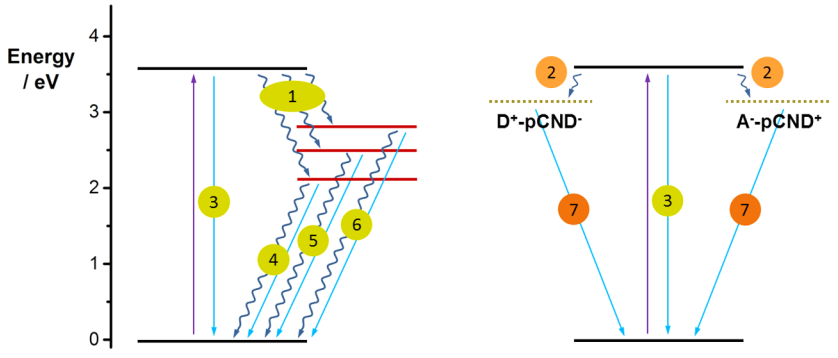

Figure 9. Energy level diagram and excited state deactivation pathways for pCND (left) and for pCND in conjunction with a donor/acceptor (right).

dx.doi.org/10.1021/ja510183c | J. Am. Chem. Soc. 2014, 136, 17308–17316

the binding constants for pCNDs with MV^{2+} and TEOA were determined by fitting the F/F_0 versus MV^{2+} or TEOA concentration plots with functions based on a bimolecular theory. The correspondingly determined binding constants are 2 orders of magnitude lower for TEOA than for MV^{2+}; see Figures S29−30. We attribute these differences to the absence of electrostatic interactions between pCNDs and TEOA. Furthermore, the quenching leads to a red shift of 3 nm of the luminescence maximum, which contrasts with the blue shift seen in the luminescence quenching with MV^{2+}, Figures S31−32.

As above, the dynamics of the quenching process were studied by means of time-resolved techniques. In TCSPC experiments, the TEOA-induced quenching is only reflected in the ∼5 ns component. It is strongly affected by TEOA in terms of amplitude and lengths. This shows that the different observed lifetimes are indeed connected to different deactivation pathways. In terms of fluorescence up-conversion experiments, the two lifetimes of 37.2 and 669 ps give rise to an overall quenching, Figures S26 and S28.

The addition of TEOA to pCND produces a new maximum at 660 nm in the transient absorption spectra, which relates to the one electron oxidized form of TEOA; see Figure 11. Thus,

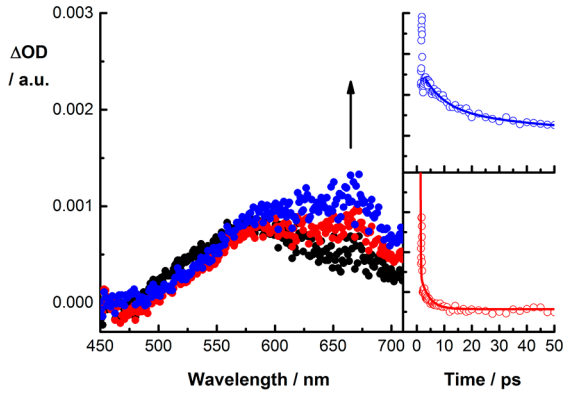

Figure 11. Left: Differential absorption spectra obtained upon femtosecond flash photolysis (387 nm) of pCND in aqueous solutions without (black), and upon addition of 0.1 M (red) and 1.0 M (blue) TEOA with time delays of 5 ps at room temperature. Right: Time-absorption profiles of the spectra shown on the left at 670 nm.

Table 3. Excited State Lifetimes of pCND in Aqueous Solutions and in the Presence of 1 M TEOA at Room Temperature[a]

1	2	3	4	5	6	7
TCSPC (λ_{ex} = 403 nm)						
			0.3 ns (10%)	1.8 ns (24%)	6.1 ns (66%)	
Fluorescence up-conversion (λ_{ex} = 387 nm)						
			670 ps (52%)			37 ps (53%)
Transient absorption (λ_{ex} = 387 nm)						
1.0 ps (7%)	5.6 ps (45%)					43 ps (48%)

[a]The numbers in the top line are analogous to Figure 9.

detection of the 660 nm transient confirms that the quenching occurs through photoinduced electron transfer. Again, fitting the transient decays at, for example, 670 nm yields three lifetimes; see Table 3. Upon stepwise addition of TEOA, the intermediately lived (5.7 ± 0.7 ps) and the long-lived (37 ± 5.0 ps) components dominate the decays. Therefore, we assign these two components to charge separation and charge recombination, respectively.

CONCLUSIONS

We have presented a novel method to produce pCNDs with a narrow, excitation-independent luminescence that constitute a valuable reference substance for the photophysics of light-emitting carbon nanomaterials in general.

A theoretical analysis of the optical properties of solvated, functionalized sp^2-networks shows that even a perfectly monodisperse sample with only intrinsic luminescence would feature a broad emission band. At the same time, chemical modifications and changes in size also lead to changes in emission wavelengths and lifetimes. The comparison of simulated and experimental luminescence decay curves reveals that intrinsic luminescence from sp^2-carbon networks is a plausible explanation for the emission at short wavelengths, but that other deactivation pathways dominate the luminescence at longer wavelengths.

We have further shown that pCNDs act either as electron donors or as electron acceptors, when combined with, for example, electron accepting MV^{2+} and electron donating TEOA, respectively. Their negative surface charges and effective charge-transfer properties, especially with MV^{2+}, render pCNDs a valuable building block in the self-assembly of hybrids. This is currently under investigation in our laboratory. Finally, we would like to stress that our study shows that CNDs differ from inorganic quantum dots in many respects. Interpretation of experimental observations by analogy to inorganic quantum dots is tempting but often over-simplifying.

EXPERIMENTAL SECTION

Citric acid (99.5%) was used as received from Sigma-Aldrich. Urea (99.5%) was used as received from Merck. Millipore water was used for the preparation of the solutions. Reactions were conducted in an Initiator$^+$ Microwave reactor (Biotage) in 20 mL vials. Emission spectra were recorded with a Fluoromax 3 (Horiba) spectrofluorometer. UV/vis absorption spectra were recorded with Lambda 2 (PerkinElmer) or Cary5000 (Varian). All steady state spectra were recorded at room temperature using 10 mm path-length cuvettes. Fluorescence quantum yields were determined by the gradient method using Coumarin 1 (ϕ_f = 0.055 in H_2O)[22] as a standard. Time-correlated single-photon counting measurements were recorded with a FluoroLog-3 lifetime spectro-fluorometer (Horiba) supplied with an integrated TCSPC software. Sample excitation was accomplished with a nano-LED-295L. Femtosecond transient absorption studies and femtosecond fluorescence up-conversion were performed with 387 nm laser pump pulses (1 kHz, 150 fs pulse width) from an amplified Ti:sapphire laser system (Clark-MXR, Inc.). All spectra were recorded in 2 mm quartz (OS) cuvettes at ambient conditions. High-resolution transmission electron microscopy was carried out with an aberration-corrected Titan^3 80−300 (FEI Company) at an acceleration voltage of 200 kV. The samples were prepared by dipping TEM grids (ultrathin carbon film on holey carbon support, Ted Pella, Inc.) into the prepared solutions. Subsequent drying was performed in a desiccator.

^{1}H and ^{13}C NMR spectra (liquid and solid state) were recorded on a JEOL Alpha500 spectrometer. For the solid state spectra, a 6 mm rotor has been used. Detailed spectral parameters are given in the Supporting Information.

The height of the CNDs was measured with an AFM (NanoWizard 3 from JPK Instruments, Berlin, Germany). The resolution was set to

dx.doi.org/10.1021/ja510183c | J. Am. Chem. Soc. 2014, 136, 17308−17316

1024 pixels × 1024 pixels for a measured surface of 2.5 × 2.5 μm^2 (~2.44 nm/pixel). For imaging, intermittent contact mode with a NSC15/AlBS probe (frequency 325 kHz, spring constant 46 N/m and nominal tip radius <10 nm) applying a slow scan rate of 0.8 Hz in combination with a relatively high set point of 750 mV and low PGain of 0.01 was performed. Prior to AFM-measurement the CND were dispersed in water (concentration of few mg/mL) and subsequently coated on a silicon wafer. For data evaluation JPK Data Processing Software version spm-4.2.58 was used for image processing. The obtained AFM-images were analyzed by contrast imaging in Gwyddion 2.36. To identify the Nano dots a threshold value for the height was set corresponding to 15% contrast relative to the background caused by the roughness of the wafer. All heights below the threshold value are attributed to wafer roughness. The found height corresponds to the measured height in comparison to the average surface height.

A modified preparative centrifuge, type Optima L-90K from Beckman Coulter, was used for the SV-AUC experiments. Detailed information regarding the hardware and data acquisition can be found in the literature.[23] Two-sector titanium centerpieces from Nanolytics, Germany, with a path length of 12 mm were used for the experiments. SV data was acquired every 2 min at 55 000 rpm for 30 h, 25 °C and a radial resolution of 50 μm. Water was used as a solvent and density was 997.13 kg m^{-3} and viscosity was 0.891 mPas. Multiwavelength intensity data were recorded and converted to absorbance data. Data at a wavelength of 342 nm were used for hydrodynamic analysis. Data evaluation was carried out using the software Ultrascan3 including 2-dimensional spectrum analysis (2DSA) and Monte Carlo (MC) analysis to calculate the 95% confidence levels—Figure 9.[24] During the MC iterations, synthetic noise is generated and applied to the fit to calculate the statistic parameters for s and D best. The 95% confidence intervals determined were $[-0.164, 0.636] \times 10^{-13}$ s for s and [6.337, 7.560] × 10^{-6} cm^2 s^{-1} for D. Broader confidence intervals were obtained for s compared to D due to the very slow sedimentation process, which makes an accurate determination of s challenging. However, pCNDs were measured twice and the results showed a very good reproducibility with deviations less than 3% for the average values of s and D. Details regarding the 2DSA-MC can also be found in literature.[25] All values for s and D provided in the manuscript were converted to standard conditions for water at 20 °C.

DFT calculations were performed at the ωB97X-D/def2-SV(P) level for the monomers and at B97D/def2-SV(P) level for the bilayer, using Gaussian09. MD simulations were performed using the COMPASS force field and NPT ensemble at room temperature and ambient pressure with Forcite.[26] Semiempirical UNO-CIS calculations were performed using the PM3 Hamiltonian as implemented in VAMP 11. For these calculations, solvation was accounted for via the self-consistent reaction field method.[27]

Fluorescence spectra and decays were calculated according to the approach of Beierlein, Clark et al.[28] Specifically, A_{21} coefficients were calculated from the transition dipole moments $|M_{12}|$ of S1 states using the following formula:

$$A_{21} = \frac{16\pi^3\nu^3}{3h\varepsilon_0 c^3}|M_{12}|^2$$

with the frequency ν, the dielectric constant ε_0, Planck's constant h and the speed of light c. Nonradiative decay constants k_{nr} were calculated from the quantum yield ϕ according to

$$k_{nr} = \frac{k_r}{\phi} - k_r$$

Fluorescence decay curves for all states were simulated via the following:

$$I(t) = e^{-(k_r+k_{nr})t}$$

All states were broadened by a fwhm = 20.0 nm Gaussian function.

■ ASSOCIATED CONTENT

Supporting Information

Additional figures and tables, as referenced in the text. This material is available free of charge via the Internet at http://pubs.acs.org.

■ AUTHOR INFORMATION

Corresponding Author

dirk.guldi@fau.de

Author Contributions

#V.S. and J.T.M. contributed equally.

Notes

The authors declare no competing financial interest.

■ ACKNOWLEDGMENTS

This work was supported by the Deutsche Forschungsgemeinschaft as part of the Excellence Cluster "Engineering of Advanced Materials" and the Collaborative Research Centre SFB 953 "Synthetic Carbon Allotropes". The Bayerische Staatsregierung is also kindly acknowledged for funding granted as part of the "Solar Technologies go Hybrid" initiative. Johannes T. Margraf is supported by a Beilstein Foundation Scholarship. Volker Strauss is supported by the "Universität Bayern e.V." We would like to thank Marion Bartesch for help with the XRD, Christian Oelsner for help with the Fluorescence Upconversion and Ricarda Schäfer for the TGA-MS measurements.

■ REFERENCES

(1) Li, H.; Kang, Z.; Liu, Y.; Lee, S.-T. *J. Mater. Chem.* **2012**, *22*, 24230−24253.

(2) Wang, L.; Zhu, S.-J.; Wang, H.-Y.; Wang, Y.-F.; Hao, Y.-W.; Zhang, J.-H.; Chen, Q.-D.; Zhang, Y.-L.; Han, W.; Yang, B.; Sun, H.-B. *Adv. Opt. Mater.* **2013**, *1*, 264−271.

(3) Schäfer, R. A.; Englert, J. M.; Wehrfritz, P.; Bauer, W.; Hauke, F.; Seyller, T.; Hirsch, A. *Angew. Chem., Int. Ed.* **2013**, 754−757.

(4) Cao, L.; Wang, X.; M, J.; Fushen, Lu; Wang, H.; Luo, P. G.; Lin, Y.; Harruff, B. A.; Veca, L. M.; Murray, D.; Xie, S.-Y.; Sun, Y.-P. *J. Am. Chem. Soc.* **2007**, *129*, 11318−11319.

(5) Chen, B.; Li, F.; Li, S.; Weng, W.; Guo, H.; Guo, T.; Zhang, X.; Chen, Y. T.; Hong, X.; You, S.; Lin, Y.; Zeng, K.; Chen, S. *Nanoscale* **2013**, *5*, 1967−1971.

(6) Kwon, W.; Do, S.; Lee, J.; Hwang, S.; Kim, J. K.; Rhee, S.-W. *Chem. Mater.* **2013**, *25*, 1893−1899.

(7) Wang, X.; Cao, L.; Lu, F.; Meziani, M. J.; Li, H.; Qi, G.; Zhou, B.; Harruff, B. A.; Kermarrec, F.; Sun, Y. P. *Chem. Commun.* **2009**, 3774−3776.

(8) Xu, Y.; Wu, M.; Feng, X.-Z.; Yin, X.-B.; He, X.-W.; Zhang, Y.-K. *Chem.—Eur. J.* **2013**, *19*, 6282−6288.

(9) Das, S. K.; Liu, Y.; Yeom, S.; Kim, D. Y.; Richards, C. I. *Nano Lett.* **2014**, *14*, 620−625.

(10) Wang, L.; Zhu, S.-J.; Wang, H.-Y.; Qu, S.-N.; Zhang, Y.-L.; Zhang, J.-H.; Chen, Q.-D.; Xu, H.-L.; Han, W.; Yang, B.; Sun, H.-B. *ACS Nano* **2014**, *8*, 2541−2547.

(11) Xue, Q.; Huang, H.; Wang, L.; Chen, Z.; Wu, M.; Li, Z.; Pan, D. *Nanoscale* **2013**, *5*, 12098−12103.

(12) Li, X.; Lau, S. P.; Tang, L.; Ji, R.; Yang, P. *Nanoscale* **2014**, *6*, 5323−5328.

(13) Sun, Y.-P.; Zhou, B.; Lin, Y.; Wang, W.; Fernando, K. A. S.; Pathak, P.; Meziani, M. J.; Harruff, B. A.; Wang, X.; Wang, H.; Luo, P. G.; Yang, H.; Kose, M. E.; Chen, B.; Veca, L. M.; Xie, S.-Y. *J. Am. Chem. Soc.* **2006**, *128*, 7756−7757.

(14) Li, L.-S.; Xin Yan, X. *J. Phys. Chem. Lett.* **2010**, *1*, 2572−2576.

(15) Qu, S.; Wang, X.; Lu, Q.; Liu, X.; Wang, L. *Angew. Chem., Int. Ed.* **2012**, *51*, 12215−12218.

(16) Walter, J.; Nacken, T. J.; Damm, C.; Thajudeen, T.; Eigler, S.; Peukert, W. *Small* **2014**, DOI: 10.1002/smll.201401940.
(17) Weigend, F.; Ahlrichs, R. *Phys. Chem. Chem. Phys.* **2005**, *7*, 3297−3305.
(18) Chai, J.-D.; Head-Gordon, M. *Phys. Chem. Chem. Phys.* **2008**, *10*, 6615−6620.
(19) Dral, P. O.; Clark, T. *J. Phys. Chem. A* **2011**, *115*, 11303−11312.
(20) Stewart, J. J. P. *J. Mol. Model.* **2007**, *13*, 1173−1213.
(21) Kaim, W.; Fiedler, J. *Chem. Soc. Rev.* **2009**, *38*, 3373−3382.
(22) Jones, G., II.; Jackson, W. R.; Choi, C. Y.; Bergmark, W. R. *J. Phys. Chem.* **1985**, *89*, 294−300.
(23) Walter, J.; Löhr, K.; Karabudak, E.; Reis, W.; Mikhael, J.; Peukert, W.; Wohlleben, W.; Cölfen, H. *ACS Nano* **2014**, *8*, 8871−8886.
(24) Demeler, B.; Nguyen, T.-L.; Gorbet, G. E.; Schirf, V.; Brookes, E. H.; Mulvaney, P.; El-Ballouli, A. a. O.; Pan, J.; Bakr, O. M.; Demeler, A. K.; Hernandez Uribe, B. I.; Bhattarai, N.; Whetten, R. L. *Anal. Chem.* **2014**, *86*, 7688−7695.
(25) Demeler, B.; Brookes, E. *Colloid Polym. Sci.* **2008**, *286*, 129−137.
(26) Sun, H. *J. Phys. Chem. B* **1998**, *102*, 7338−7364.
(27) Rauhut, G.; Clark, T.; Steinke, T. *J. Am. Chem. Soc.* **1993**, *115*, 9174−9181.
(28) Beierlein, F. R.; Othersen, O. G.; Lanig, H.; Schneider, S.; Clark, T. *J. Am. Chem. Soc.* **2006**, *128*, 5142−5152.
(29) Jiang, Z.; Nolan, A.; Walton, J. G. A.; Lilienkampf, A.; Zhang, R.; Bradley, M. *Chem.—Eur. J.* **2014**, *20*, 10926−10931.
(30) Qian, Z.; Ma, J.; Shan, X.; Feng, H.; Shao, L.; Chen, J. *Chem.—Eur. J.* **2014**, *20*, 2254−2263.
(31) Ghosh, S.; Chizhik, A. M.; Karedla, N.; Dekaliuk, M. O.; Gregor, I.; Schuhmann, H.; Seibt, M.; Bodensiek, K.; Schaap, I. A. T.; Schulz, O.; Demchenko, A. P.; Enderlein, J.; Chizhik, A. I. *Nano Lett.* **2014**, *14*, 5656−5661.
(32) Newell, J. A.; Edie, D. D.; Fuller, E. L. *J. Appl. Polym. Sci.* **1996**, *60*, 825−832.
(33) Lewis, I. C. *Carbon* **1982**, *20*, 519−529.
(34) Jing, M.; Wang, C.; Wang, Q.; Bai, Y.; Zhu, B. *Polym. Degrad. Stab.* **2007**, *92*, 1737−1742.
(35) Schaber, P. M.; Colson, J.; Higgins, S.; Thielen, D.; Anspach, B.; Brauer, J. *Thermochim. Acta* **2004**, *424*, 131−142.